Desalination and Water Treatment
www.deswater.com
doi: 10.5004/dwt.2021.27416

230 (2021) 169–183
August

Facile solid-state synthesis of heterojunction CeO_2/TiO_2 nanocomposite as an efficient photocatalyst for the degradation of organic pollutants

Muhammad Zobayer Bin Mukhlish, Md. Amirul Islam, Md Anisur Rahman, Shafiul Hossain, Md. Akhtarul Islam, Md. Tamez Uddin*

Department of Chemical Engineering and Polymer Science, Shahjalal University of Science and Technology, Sylhet 3100, Bangladesh, emails: mtuddin_cep@yahoo.com/mtuddin-cep@sust.edu

Received 26 October 2020; Accepted 9 May 2021

ABSTRACT

In this study, CeO_2/TiO_2 nanocomposites (NCs) were synthesized by adopting a straightforward two steps method comprising, first, the synthesis of CeO_2 and TiO_2 nanoparticles by wet chemical precipitation method and second, the heterostructure CeO_2/TiO_2 NCs by solid-state reaction process. The CeO_2/TiO_2 NCs were characterized by X-ray diffraction, N_2 adsorption–desorption isotherm analysis, field emission scanning electron microscopy, energy-dispersive X-ray spectroscopy, and UV-vis diffuse reflectance spectroscopy. Regardless of CeO_2 content, the bandgap energies of CeO_2/TiO_2 NCs were lower than that of pure TiO_2. Photocatalytic activity of the synthesized photocatalysts was assessed by degrading a model dye methylene blue under the illumination of UV light. The CeO_2/TiO_2 NCs containing 2 wt% CeO_2 exhibited higher photocatalytic degradation efficiency compared to reference TiO_2 (P25), pure TiO_2, and CeO_2/TiO_2 NCs containing CeO_2 other than 2 wt%. The alkaline environment was favorable for photocatalytic decomposition of cationic dye methylene blue (MB). The enhanced degradation efficiency of CeO_2/TiO_2 NCs was substantiated in terms of vectorial charge separation and the reduction of photogenerated charge carriers owing to the band offsets existing at the interface between CeO_2 and TiO_2 NPs. Finally, no significant change in the degradation efficiency of CeO_2/TiO_2 NCs after successive uses evidenced the stability and reusability of the photocatalysts. Therefore, it can be concluded that the synthesized CeO_2/TiO_2 heterostructure photocatalyst would be a promising candidate for application in wastewater treatment.

Keywords: Solid state synthesis; CeO_2/TiO_2 nanocomposites; Heterojunction photocatalyst; Degradation efficiency; Band offset

1. Introduction

Safe and clean water is important for human health and pleasure, ecosystems, and also for a booming economy [1]. With the rapid urbanization and industrialization, more and more toxic and harmful pollutants are entering into the water through various channels, which directly or indirectly threaten the harmonious development of the ecological environment and humanity [2]. Organic dyes are considered as one of the major contaminants discharged into the water environment from various industries like textiles, leather, food, pharmaceutical, printing, etc. [3,4]. Dyes tend to suppress photosynthetic activity in aquatic habitats by preventing the penetration of sunlight that affects the aquatic biota [5]. Moreover, azo dyes, which constitute about 60%–70% of the textile dyestuffs, have genotoxic, mutagenic, and carcinogenic effects on living beings [6]. Consequently, the treatment of wastewater containing such ecotoxic dyes is of great interest to ensure the sustainability of the environment for future generations.

The conventional techniques like coagulation, membrane separation, adsorption, and activated sludge process

* Corresponding author.

are not effective enough to treat organic containing effluent released from different industries as most of these techniques create secondary pollutions [7–12]. In recent decades, advanced oxidation processes (AOPs) have drawn much attention for the treatment of wastewater as these techniques completely degrade the toxic organic matters in the wastewater or convert the organic matters into less harmful products [13–15]. Among AOPs, heterogeneous photocatalysis using semiconductor metal oxides has been proved to be a promising alternative, economical, and harmless technology for complete mineralization of toxic organic pollutants to H_2O and CO_2 as end products [16–18]. Since the discovery of titanium oxide (TiO_2) as a photocatalyst for water splitting [19], it has been extensively using as a photocatalyst for the degradation of pollutants in industrial wastewaters due to its stability, photoactivity, low cost, and non-toxicity to living organisms [20–23]. Nevertheless, the industrial use of TiO_2 is constrained due to the rapid recombination of the photogenerated charges [24]. Therefore, the great challenge of the practical application of TiO_2 for the degradation of organics is to reduce the recombination of photogenerated charge carriers.

Over the past decades, researchers have adopted different strategies to enhance the photocatalytic activity of TiO_2 [25–31]. One of the most effective strategies is to develop heterostructure photocatalysts by coupling TiO_2 with either n-type metal oxide semiconductors or p-type metal oxide semiconductors making n–n heterojunction [32] and p–n heterojunction [33,34], respectively. Recently, enhanced photocatalytic activity of various TiO_2 based heterostructure photocatalysts, like NiO/TiO_2 [33,35], SnO_2-TiO_2 [36,37], TiO_2/ZnO [38], RuO_2/TiO_2 [39], Fe_2O_3-TiO_2 [40–42], ZrO_2/TiO_2 [43], and CdS-TiO_2 [44], have been studied for the degradation of organic pollutants in water. Cerium oxide (CeO_2) is an n-type semiconductor with a moderate bandgap (3.0–3.6 eV) [45]. CeO_2 has a fluorite structure and Ce^{4+} in CeO_2 is smaller to stabilize the fluorite structure [46]. Ce can exist as Ce^{4+} and Ce^{3+}. Some of the Ce^{4+} is reduced to Ce^{3+} and is accompanied by the release of oxygen creating oxygen vacancies. Thus, the photocatalytic activity of pure CeO_2 is low and cannot be applied to degrade organic pollutants; because the formed oxygen vacancies act as recombination centers of photo-generated charges [47]. However, the coupling of CeO_2 with other semiconductors having appropriate band positions can improve the photocatalytic activity of both pristine semiconductors. In coupled semiconductors, the recombination of photogenerated charges is reduced by spatial transfer of charges to the conduction band (CB) and valence band (VB) of two different semiconductors in opposite directions. The direction of charge transfer depends on the positions of CB and VB of the constituent semiconductors. It is reported that CB and VB positions of TiO_2 are more positive than those of CeO_2 [48–52]. Thus, there exist valence band and conduction band offsets at the interface between CeO_2 and TiO_2 of heterojunction CeO_2/TiO_2 nanoparticles that suppress the charge recombination by transferring them in opposite direction leading to the improved activity of CeO_2/TiO_2 photocatalyst for the degradation of organic pollutants. However, the actual degradation efficiency of the heterostructure CeO_2/TiO_2 photocatalysts depends on the preparation method and the optimum content of CeO_2 [53]. In this context, a number of researchers have attempted to prepare CeO_2/TiO_2 photocatalysts by different methods like hydrothermal [54,55], sol-gel [53,56,57], and impregnation [58]. The as-prepared heterostructure CeO_2/TiO_2 photocatalysts exhibited higher degradation efficiencies for organic pollutants under the irradiation of UV and visible light. Different synthetic methods of heterostructure CeO_2/TiO_2 photocatalysts and their degradation efficiencies for the degradation of different organic dyes are shown in Table S1. However, most of the current methods for the synthesis of heterostructure photocatalyst are primarily based on the solution method, which is rather complicated and apparatus-dependent. The preliminary study in our laboratory showed that the photocatalytic activity of CeO_2/TiO_2 NC prepared by precipitating CeO_2 onto the surface of TiO_2 nanoparticles was drastically reduced. This might be due to the formation of CeO_2 film on the TiO_2 surface which prevented the activation of TiO_2 by inhibiting the penetration of light. To avoid such unwanted phenomena, some researchers have synthesized heterostructure nanocomposites by solid-state sintering method [59–62]. It is a simple, easy, and straightforward method to prepare nanocomposites on an industrial scale. To the best of our knowledge, no work has been reported yet on the synthesis of heterostructure CeO_2/TiO_2 NCs by the solid-state sintering method.

In the present study, heterostructure CeO_2/TiO_2 NCs containing different amounts of CeO_2 were successfully prepared by a straightforward solid-state sintering method. The synthesized NCs were then analyzed with different characterization techniques. The photocatalytic degradation efficiency of synthesized NCs was evaluated by degrading of MB dye under the illumination of UV light. The mechanism of improved photocatalytic performance was attributed to enhanced charged separation owing to band discontinuity at the interface of CeO_2/TiO_2 NCs.

2. Materials and methods

2.1. Chemicals and reagents

Analytical grade reagents were bought and used as received in order to prepare TiO_2, CeO_2, CeO_2/TiO_2 NCs. Titanium(IV) tetrachloride and 25 wt% aqueous ammonia were obtained from Merck (Germany). Cerium nitrate hexahydrate was purchased from Sigma Aldrich (Germany). Methylene Blue (MB) ($C_{16}H_{18}ClN_3S$) was collected from Loba Chemie, India. The solutions of the desired pH were obtained by adding a suitable amount of dilute HCl and NaOH solutions.

2.2. Synthesis of nanoparticles

2.2.1. Synthesis of TiO_2 NPs

The TiO_2 NPs were synthesized by precipitation method using titanium(IV) chloride and aqueous ammonia (25%) solution as precursor and precipitant, respectively. In a typical method, 2 mL titanium(IV) chloride was mixed with 10 mL distilled water and was stirred for 30 min. Subsequently, an aqueous ammonia solution was added to the titanium(IV) chloride solution to form a precipitate

of titanium hydroxide. The precipitate was then separated from the mother solution by centrifugation and washed with deionized water to obtain chlorine-free solid mass. The possible reaction scheme for the above synthesis could be proposed as:

$$NH_4OH \Leftrightarrow NH^+_{4(aq)} + OH^-_{(aq)} \quad (1)$$

$$TiCl_4 \rightarrow Ti^{4+}_{(aq)} + 4Cl^-_{(aq)} \quad (2)$$

$$Ti^{4+}_{(aq)} + 4OH^-_{(aq)} \Leftrightarrow Ti(OH)_{4(s)} \quad (3)$$

The obtained solid mass of titanium hydroxide were then dried at 110°C for 12 h followed by calcination at 500°C in a muffle furnace in presence of atmospheric oxygen for 2 h to get crystalline TiO_2 powder. During calcination in the furnace, the titanium hydroxide is dehydrated to TiO_2 by the following chemical transformation:

$$Ti(OH)_{4(s)} \xrightarrow{\Delta} TiO_{2(s)} + 2H_2O_{(v)} \quad (4)$$

The TiO_2 so obtained was ground to powder with mortar-pestle and was stored in an air-tight container for further experiment. The TiO_2 powder so obtained will be called pure TiO_2 from now onward.

2.2.2. Synthesis of CeO_2 NPs

The CeO_2 nano-powders were synthesized by the precipitation method using cerium(III) nitrate hexahydrate as precursor and ammonia solution (25%) as the precipitant. In the experimental process, 4.342 g cerium(III) nitrate hexahydrate was dissolved in 100 mL deionized water. Dropwise addition of ammonia solution to the above solution under magnetic stirring at room temperature gave precipitate of cerium (IV) hydroxide. The suspension was aged overnight at 25°C under continuous stirring. The resultant light yellow colored precipitate of $Ce(OH)_4$ was washed with deionized water several times and was separated from the suspension by centrifugation at 5,000 rpm. The so-obtained wet particles were then dried at 110°C overnight and subsequently calcined at 500°C for 2 h to obtain CeO_2 crystals. The CeO_2 powder was then ground with agate mortar-pestle and stored for further use.

2.2.3. Preparation of CeO_2/TiO_2 heterostructure nanocomposites

The CeO_2/TiO_2 heterostructure photocatalysts were prepared by the solid-state sintering method. In a typical method, 0.005 g CeO_2 and 0.245 g TiO_2 (i.e., CeO_2:TiO_2 = 2:98) were thoroughly mixed and ground in a mortar for 40 min through the agate mortar and pestle. The ground powder was then calcined at 500°C for 2 h in a furnace. The heat treatment enhanced the chemical binding among the particles and strengthened the mechanical properties of the CeO_2/TiO_2 NC [63]. The obtained NC was then labeled as 2 wt% CeO_2/TiO_2 and stored for further use. The CeO_2/TiO_2 NCs containing other weight percentages of CeO_2 were prepared by the same procedure with the corresponding CeO_2/TiO_2 ratio.

2.3. Characterizations of NPs

The crystallinity of the prepared NPs was investigated using an X-ray diffractometer (model 3040XPert PRO, Philips). The 2θ data were obtained using a continuous scan mode in the 2θ range of 10°–80°. The mean size of the crystallites was calculated using Scherrer's formula. Field emission scanning electron microscopy (FESEM; JSM-7600F, JEOL, Japan) equipped with EDS was used to investigate elemental analysis and surface morphology of CeO_2/TiO_2 NCs. The bandgap energy of the prepared NPs was determined by measuring UV-vis diffuse reflectance spectra (UV-vis DRS) of the NPs at ambient conditions. The UV-vis DRS was recorded by scanning the samples in wavelength ranging from 200 to 800 nm with a UV-vis-NIR spectrometer (LAMDA 750, PerkinElmer, Inc, USA) using sintered PTFE as a standard reference. The nitrogen adsorption-desorption isotherms of the prepared photocatalysts were recorded at 77 K by a porosimetry analyzer (ASAP 2020 Plus, Micromeritics Instrument Corporation, USA). Before executing measurements, the NP samples were degassed at 120°C under ultra-high vacuum for 10 h. The specific areas (S_{BET}) were estimated through the Brunauer–Emmett–Teller (BET) equation and the pore size distributions were evaluated from the adsorption courses of the nitrogen adsorption-desorption isotherms by using the Barrett, Joyner, Halenda (BJH) method.

The point of zero charges (pH_{PZC}) of the synthesized NPs was obtained by the pH drift method [64]. At first, eight samples of 200 mL 0.1 M KNO_3 solution were prepared as a background electrolyte. The role of background electrolyte KNO_3 was to adjust the ionic strength of the solution to a constant value of 0.1 M. The initial pH of the electrolyte solution was adjusted in the range 4–12 with the addition of the suitable amount of 0.1 M HCl or 0.1 M NaOH solution. 100 mg of CeO_2/TiO_2 NCs was added to 200 mL solutions of different pH and shaken for 24 h. Then the final pH (pH_{final}) was measured. The difference between the initial and final solution pH, ΔpH (= $pH_{initial}$ – pH_{final}) was plotted against the initial pH, and the pH corresponding to the ΔpH value of zero was considered as the pHpzc of the NC surface.

Complete mineralization of MB dye was tested by determining chemical oxygen demand (COD) of the MB solution after photocatalytic degradation using a photometer (photometer MD 600, Lovibond, Germany) according to the procedure described elsewhere [65].

2.4. Photocatalytic experiment

The photocatalytic activities of the prepared CeO_2/TiO_2 NCs, pure TiO_2, and commercial TiO_2 (Degussa, P-25) were investigated by degrading MB under the radiation of a mercury lamp (Model: MBFU 125W E27, OSRAM). The photodegradation tests were conducted by placing a UV lamp horizontally over a 500 mL glass beaker. The reaction cell was maintained at 25°C by circulating water. In the photocatalytic experiment under air atmosphere, 100 mL solution of MB (10 mg/L) at pH 8 containing 0.1 g photocatalyst was stirred in dark for 30 min prior to illumination. 4 mL of

the suspensions were collected as a sample after a predetermined time interval of light irradiation and the concentration of MB in the supernatant after centrifugation was analyzed by a UV-vis spectrophotometer (UV-1650, SHIMADZU, Japan) measuring absorbance at 664 nm. An experiment in absence of UV light irradiation was also conducted as blank with 2 wt% CeO_2/TiO_2 catalyst. Another blank experiment without the photocatalyst but with UV irradiation on MB solution was also performed.

3. Results and discussion

3.1. Characterization of NPs

3.1.1. XRD analysis

XRD analysis is performed to examine the crystallinity and the size of the synthesized NPs. The major diffraction lines shown in Fig. 1A at 2θ = 25.29°, 37.85°, 48.05°, 54.05°, 55.14°, and 62.84° are ascribed to the (101), (004), (200), (105), (211), and (204) planes of anatase phase TiO_2, respectively (JCPDS card No. 21-1272) [33,66]. No characteristic diffraction peaks of CeO_2 are visible in the spectra (a) of Fig. 1A, which is natural as the sample represents pure TiO_2. Parallel to that, spectra (b), (c), and (d) of Fig. 1A also do not show any characteristic peak of CeO_2 in spite of its availability in NCs. This might owe to the very low concentration (1–3 wt%) of the component in the CeO_2/TiO_2 NCs. The diffraction lines originating from CeO_2 might be exposed if the most intense peak of TiO_2 at 2θ = 25.29° is excluded from the XRD spectra. Thus, to diffuse any confusion, the XRD spectra were plotted in the 2θ region ranging from 27 to 70° as presented in Fig. 1B. In the spectra (a) of Fig. 1B (belonging to pure TiO_2), again no new peak has appeared that could be attributed to substances other than TiO_2. In the spectra (b), (c), and (d) of Fig. 1B (belonging to CeO_2/TiO_2 NCs), however, besides the diffraction lines corresponding to TiO_2, the two additional peaks appeared at 2θ = 28.56° and 33.08° which could be assigned to (111) and (200) planes, respectively, of cubic fluorite CeO_2 (JCPDS PDF no. 34-0394) [67,68]. The intensities of these peaks corresponding to CeO_2 increased with increasing CeO_2 content in CeO_2/TiO_2 samples. This confirms the presence of CeO_2 in the heterostructure CeO_2/TiO_2 NCs. It was obvious from the XRD patterns that the CeO_2/TiO_2 NCs has consisted of anatase phase TiO_2 and cubic fluorite CeO_2 nanoparticles. The characteristic peaks of TiO_2 in both the pure TiO_2 and the CeO_2/TiO_2 NCs are identical and they represent anatase crystal phases. No noticeable change in the crystal phase has been observed in TiO_2-component by the influence of the CeO_2-component in the NC. Promnopas et al. [69] calcined TiO_2 films at 450°C and reported having detected an insignificant amount of rutile phase crystals in addition to the predominant anatase crystalline phase [69]. In this work, however, pure TiO_2 shows anatase crystalline phase only, and no transition to rutile phase is detected in CeO_2/TiO_2 NCs (both formed by calcination at 500°C).

The average crystallite sizes of TiO_2 in samples estimated from the Scherrer formula by using the (101) plane was found to be 16.97, 18.60, 18.72, and 18.92 nm in pure TiO_2, 1 wt% CeO_2/TiO_2, 2 wt% CeO_2/TiO_2, and 3 wt% CeO_2/TiO_2 samples, respectively. The size of TiO_2 crystallite increased with increasing CeO_2 content. This might be due to the deterioration of crystallinity of anatase phase TiO_2 with an increase in CeO_2 content in the NCs [68]. A similar trend in increasing crystal size of TiO_2 with CeO_2 contents was also described elsewhere [57].

3.1.2. Scanning electron microscopy and energy-dispersive X-ray spectroscopy analysis

The morphology of the CeO_2/TiO_2 NCs is investigated by FESEM images presented in Fig. 2. The FESEM images in Fig. 2A and B reveal that the TiO_2 and CeO_2 NPs in CeO_2/TiO_2 NCs are uniform in size and regular in shape.

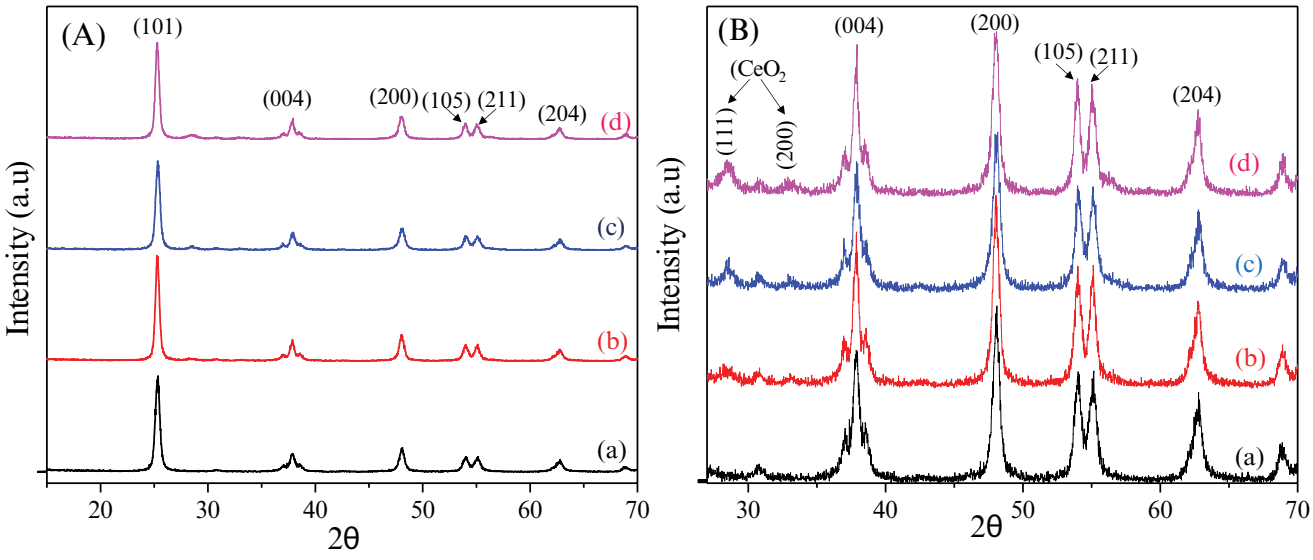

Fig. 1. XRD spectra of the synthesized TiO_2 and CeO_2/TiO_2 nanoparticles in the 2θ region of (A) 15–70°, and (B) 27–70°. (a) TiO_2, (b) 1 wt% CeO_2/TiO_2, (c) 2 wt% CeO_2/TiO_2, and (d) 3 wt% CeO_2/TiO_2.

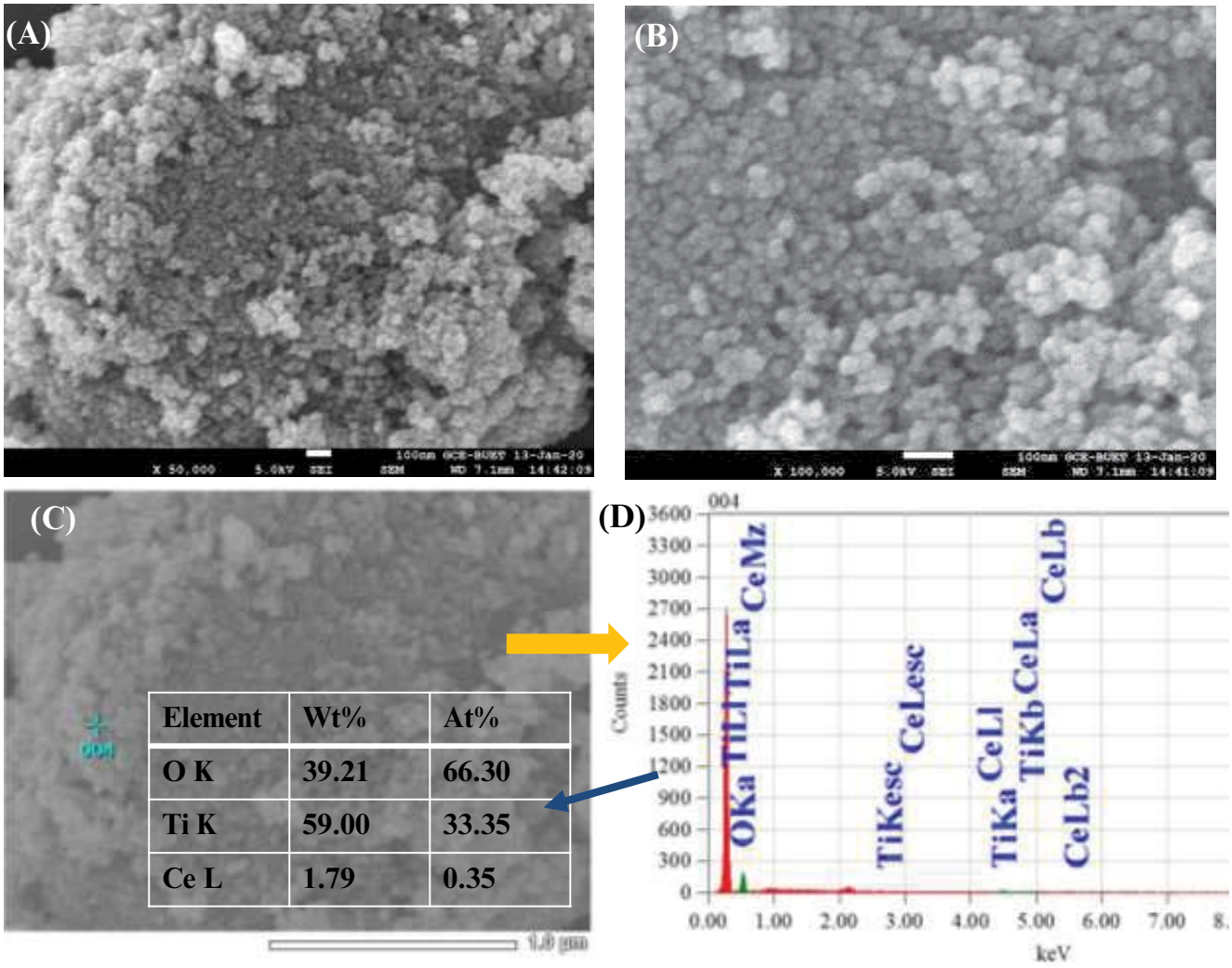

Fig. 2. FESEM images of 2 wt%CeO_2/TiO_2NCs (A and B in different magnification) and EDX analysis of 2 wt%CeO_2/TiO_2 NCs (C and D).

The images demonstrate that most of the particles formed are spherical in shape (in nano-level scale) and few of them appear as an aggregate of different shapes and sizes. The average size of the NPs determined from the FESEM image is about 23 nm.

The constituents and composition of the synthesized CeO_2/TiO_2 sample were examined by energy-dispersive X-ray (EDX) analysis and the results are presented in Fig. 2C and D. As seen in Fig. 2C, the granular distribution is similar to those observed in FESEM images in Fig. 2A and B. The EDX spectrum exhibits the peaks corresponding to Ce, Ti, and O atoms only (Fig. 2C and D). As there are no peaks other than these, it could be concluded that the synthesized sample is highly pure and free of impurities, and is composed of Ce, Ti, and O only. The elemental analysis estimates an atomic ratio of Ce:Ti = 0.35:33.35 = 1:105 in the CeO_2/TiO_2 NCs, while the theoretical atomic ratio of the same in 2 wt% CeO_2/TiO_2 is calculated as 1:95. Such deviation of 10%–11% between the theoretical and the experimental values is quite acceptable in EDX analysis, where the oxygen content is not an experimentally determined value, rather an estimated one from the balance of Ti and Ce.

3.1.3. N_2 adsorption–desorption study

The nature of the nitrogen adsorption/desorption isotherms of 2 wt% CeO_2/TiO_2 NC (Fig. 3A) is of type IV with H2 type hysteresis loop (based on IUPAC classification) in the high-pressure region (P/P_0 > 0.65), indicating the major contribution of mesopores in the pore-structure [26,70]. The H2 type hysteresis loop is the characteristic of the ink-bottle-shaped pores of the solids consisting of consolidated/unconsolidated agglomerate of spherical particles [71]. The pore size distribution curve shown in Fig. 3B reveals that the major portion of the pores in CeO_2/TiO_2 NCs is located in the mesoporous region (15–50 nm) with a mean pore diameter of 17.72 nm. A small portion of the pores are located in the microporous region (>50 nm) also, and their contribution to the pore structure increases with an increase in CeO_2 content.

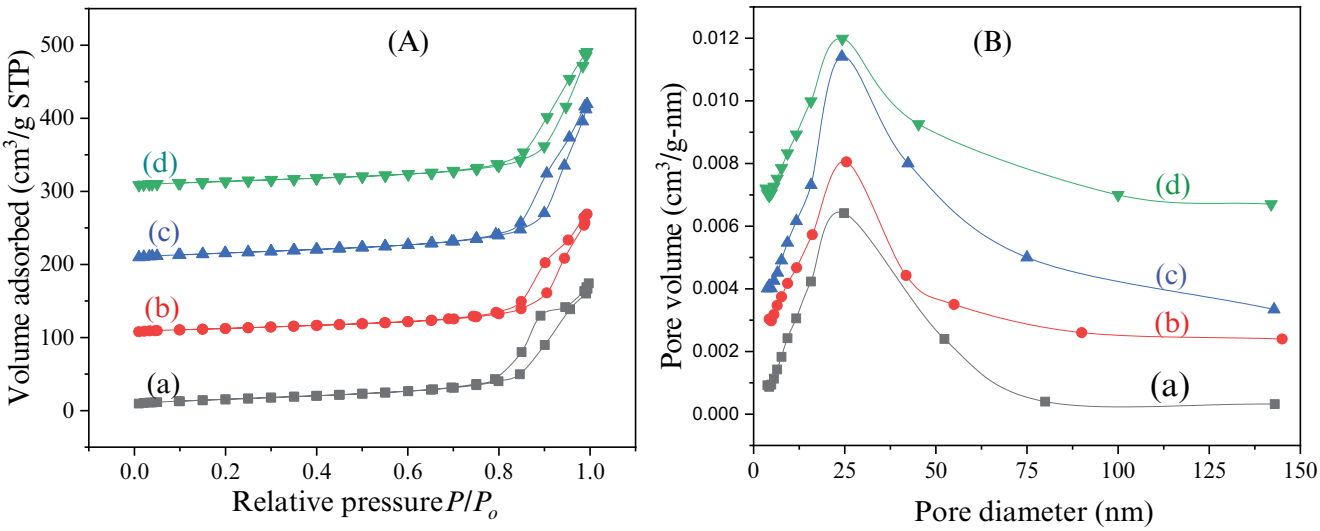

Fig. 3. (A) N_2 adsorption–desorption isotherm and (B) pore size distribution curves of the synthesized (a) TiO_2, (b) 1 wt% CeO_2/TiO_2, (c) 2 wt% CeO_2/TiO_2, and (d) 3 wt% CeO_2/TiO_2.

The textural properties, namely BET surface area (S_{BET}), total pore volume, and pore diameter of the pure TiO_2 and CeO_2/TiO_2 catalysts are given for comparison in Table 1. As seen in the Table, the S_{BET}-value does not undergo substantial changes up to 2 wt% CeO_2 in the NC, beyond which it decreases abruptly. The decrease in the BET surface area could result from the blocking of mesopore dimension when CeO_2 particles were deposited. The specific pore volume is the highest in the compositions under investigation. The average pore size increases with the increase of CeO_2 in the NCs leveling off at around 2 wt% CeO_2.

3.1.4. UV-vis DRS analysis

The optical property like the bandgap of a semiconductor plays an important role in determining its activity as a photocatalyst for the degradation of organic dyes. The UV-vis DRS was employed to inspect the optical property of the synthesized NCs as displayed in Fig. 4A. Fig. 4A demonstrates the absorption edges of pure TiO_2 at around 385 nm. Compared to that of the TiO_2 sample, the absorption edges of CeO_2/TiO_2 nanocomposites were observed to be red-shifted slightly toward a higher wavelength (inset of Fig. 4A) indicating the absorption of light more efficiently by the heterostructure CeO_2/TiO_2 NCs [72]. The Kubelka–Munk theory was used for the analysis of the diffuse reflectance spectra as given by Eq. (5) [73]:

$$F(R) = \frac{\alpha}{S} = \frac{(1-R)^2}{2R} \tag{5}$$

where $F(R)$ is the Kubelka–Munk function, R is the reflectance, α is the absorption coefficient and s is the scattering factor. The bandgap energy (E_g) of semiconductors with indirect bandgap is generally determined by Eq. (6) [74]:

$$\alpha h\nu = A\left(h\nu - E_g\right)^2 \tag{6}$$

where V and A are the light frequency and a constant, respectively. Since the scattering factor is almost wavelength-independent in some $h\nu$-range, $F(R)$ is proportional to α [75], and in this $h\nu$-range, Eq. (6) can be transformed into:

$$\left[F(R)h\nu\right]^{1/2} = B\left(h\nu - E_g\right) \tag{7}$$

where B is a constant.

For determining the optical band gap energy, E_g, a $[F(R)\cdot h\nu]^{1/2}$ vs. $h\nu$ the plot is drawn, which is an S-shaped curve. This curve contains an approximately linear section in a given $h\nu$-interval. This linear section is extrapolated to intersect the $h\nu$-axis at $h\nu = E_g$.

The calculated E_g for TiO_2 is found to be 3.22 eV which is in good agreement with the values described elsewhere [26,76,77]. The analysis reveals lower E_g of CeO_2/TiO_2 NCs compared to the pure TiO_2. The E_g for 1 wt% CeO_2/TiO_2, 2 wt% CeO_2/TiO_2, and 3 wt% CeO_2/TiO_2 have been found to be 3.14, 3.13, and 3.11 eV, respectively.

3.2. Photocatalytic degradation performance of CeO_2/TiO_2 NCs

The photocatalytic performance of the CeO_2/TiO_2 NCs is evaluated by degrading MB dye under UV light irradiation. For sake of comparison, the photocatalytic degradation of MB is monitored on the prepared anatase TiO_2 and commercial P25 as references. In addition, the photocatalytic degradation of MB under only UV light irradiation and without using photocatalyst is also investigated as a blank experiment in order to justify the degradation performance of CeO_2/TiO_2 NCs. The adsorption of MB onto CeO_2/TiO_2 NCs without light irradiation is also investigated as a blank experiment. The preliminary study shown in Fig. S1A and B demonstrate that when the solution is irradiated with UV light, the color of MB dye solution containing dispersed CeO_2/TiO_2 NCs gradually diminishes with time manifesting the breakdown of the chromophoric structure of the dye. The photocatalytic degradation kinetics

Table 1
Nitrogen sorption porosimetry studies[a] of TiO_2 and CeO_2/TiO_2 nanomaterials

Photocatalyst	S_{BET} (m^2/g)	Pore volume (cm^3/g)	Pore size (nm)
TiO_2	55.60	0.25 ± 0.01	17.73
1% CeO_2/TiO_2	55.15	0.24 ± 0.01	22.01
2% CeO_2/TiO_2	56.09	0.32 ± 0.01	23.20
3% CeO_2/TiO_2	49.52	0.28 ± 0.01	23.10

[a]Surface areas were determined by BET, pore diameters by BJH theory (applied to the adsorption branch), and pore volumes by single-point analysis

of different photocatalysts is presented in Fig. 5A in form of C/C_0 vs. t plot and Fig. 5B in form of $\ln(C/C_0)$ vs. t plot, where C is the concentration of MB at any time, t, and C_0 is its initial concentration.

Fig. 5 shows that in absence of photocatalysts, MB is not degraded at all under only UV light irradiation; or in the presence of photocatalyst without UV light irradiation. The 1 wt% CeO_2/TiO_2 and 2 wt% CeO_2/TiO_2 NCs show higher degradation efficiency compared to pure TiO_2 and commercial P-25, and the 2 wt% CeO_2/TiO_2 NC exhibit the highest photodegradation performance among all the photocatalysts tested in the present study. After 20 min of photocatalytic reaction, the degree of degradation defined as $(1 - C/C_0)$ of 1 wt% CeO_2/TiO_2, 2 wt% CeO_2/TiO_2, 3 wt% CeO_2/TiO_2, pure TiO_2, and P-25 for the degradation of MB are about 88%, 96%, 78%, 85%, and 87%, respectively. For 3 wt% CeO_2/TiO_2 NC, the excess CeO_2 might form a layer on the active surface of TiO_2 which hinders the photocatalytic activation of TiO_2 with UV light and reduce its photocatalytic degradation efficiency, and thus, 3 wt% CeO_2/TiO_2 NC shows poorer degradation capacity than 1 and 2 wt% CeO_2/TiO_2 samples [57].

It is well-known that the photodegradation reactions follow a Langmuir–Hinshelwood first-order kinetics model [84], as described by Eq. (8):

$$\ln\left(\frac{C}{C_0}\right) = -kt \tag{8}$$

where k is the reaction rate constant. If $\ln(C/C_0)$ is plotted against t, a straight line will be obtained, the slope of which is equal to the reaction rate constant, k. The experimental values of $\ln(C/C_0)$ are plotted against time, t (shown in Fig. 5B). From Fig. 5B, it is obvious that the 2 wt% CeO_2/TiO_2 NC exhibits the highest degradation efficiency with a degradation rate constant of 0.139 min^{-1}, which is about 1.54 and 3.23 times higher than those obtained with the pure TiO_2 and commercial P25, respectively. Vieira et al. [83] prepared CeO_2/TiO_2 photocatalyst by hydrothermal method for the degradation of MB under UV light irradiation and found a specific first-order rate constant of 0.04875 min^{-1} by CeO_2/TiO_2 containing 0.29 mol% Ce. A comparison of the first-order rate constant for the degradation of MB with different photocatalysts are presented in Table 2. From Table 2, it is obvious that the rate of degradation of MB with the prepared CeO_2/TiO_2 NC is very high. Therefore, the prepared CeO_2/TiO_2 NC is a promising photocatalyst for the degradation of toxic organics for environmental remediation.

Degradation efficiency largely depends on the adsorption of dye on the surface of photocatalysts as the dye molecules must be in contact with the photocatalyst to be degraded. The dye adsorption in turn depends on the solution pH. Fig. 6A exhibits the effect of pH on the photocatalytic degradation efficiency of 2 wt% CeO_2/TiO_2 NCs for the degradation of MB. As seen in Fig. 6A, the degradation efficiency is favorable in the basic medium and greatly collapses in the acidic medium. The pH dependence of the degradation efficiency could be explained with reference to the point of zero charge (pH_{PZC}) of 2 wt% CeO_2/TiO_2 NC,

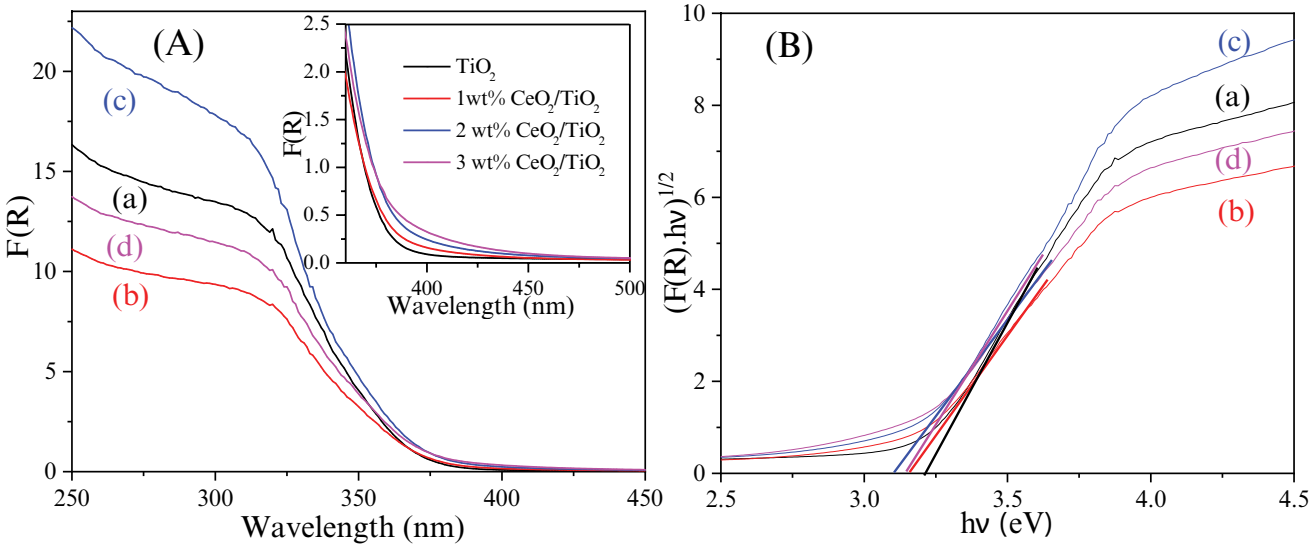

Fig. 4. (A) UV-vis DRS (Kubelka–Munk function) and (B) $(F(R)\ h\nu)^{1/2}$ vs. $h\nu$ plot for the synthesized (a) TiO_2, (b) 1 wt% CeO_2/TiO_2, (c) 2 wt% CeO_2/TiO_2, and (d) 3 wt% CeO_2/TiO_2.

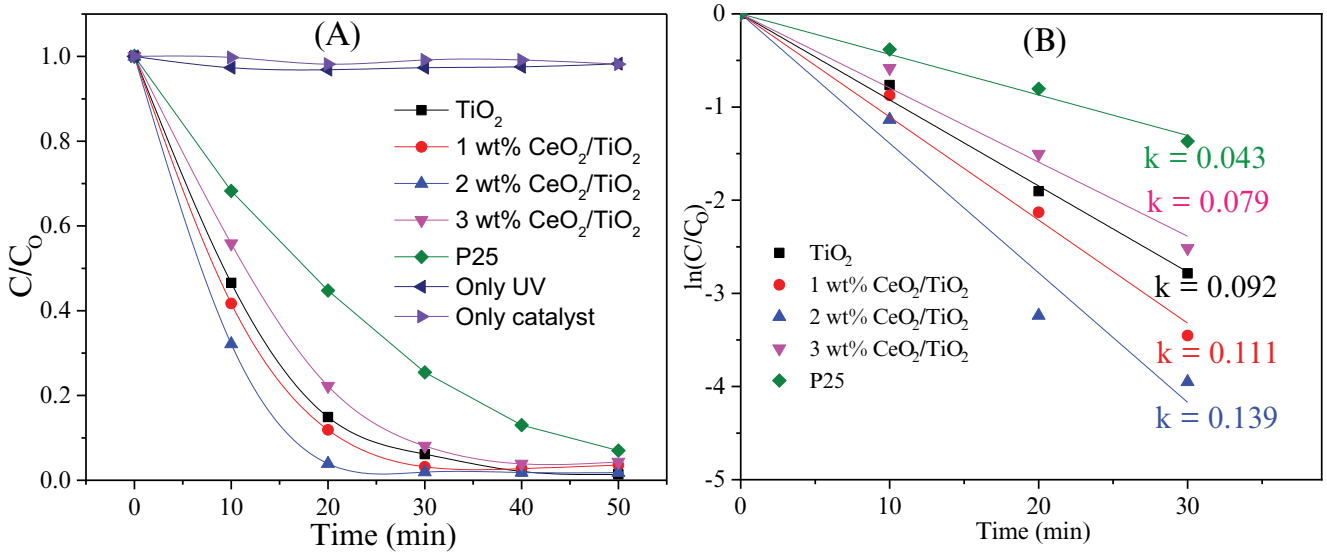

Fig. 5. Photocatalytic degradation kinetics of MB with different photocatalysts under UV light irradiation; (A) C/C_0 vs. irradiation time, t and (B) $\ln(C/C_0)$ vs. t (initial dye solution concentration = 10 mg/L; solution volume = 100 mL, pH = 8; catalyst dose = 1 g/L).

Table 2
Comparison of first-order rate constant for the degradation of MB with different photocatalysts

Photocatalyst	Organic pollutant	Catalyst and radiation dose	Rate constant k (min^{-1})	References
SnO_2–ZnO	MB	1 g/L, 125 W, 365 nm UV light	0.093	[78]
RuO2–ZnO	MB	1 g/L, 125 W, 365 nm UV light	0.106	[79]
1.25 mol% Ag/ZnO	MB	0.1 g/L, 40 W, 310 nm UV light	0.029	[80]
TiO_2/SnO_2	MB	UV light	0.004	[37]
10 wt%-Fe_2O_3/TiO_2	MB	1 g/L, 254 nm UV light	0.042	[81]
$ZnO/NiFe_2O_4$	MB	1.5 g/L, 360 nm UV light	0.989	[82]
CeO_2/TiO_2	MB	0.5 g/L, 41 W, 368 nm UV light	0.0487	[83]
2 wt% CeO_2/TiO_2	MB	1 g/L, 125 W, UV light	0.139	Present work

which is determined to be 7.60 (Fig. S2A). At pH greater than 7.60, the surface of the photocatalyst becomes negatively charged and that favors the adsorption of cationic dye MB leading to an increase in degradation efficiency. However, degradation efficiency drastically decreases at pH 12. It is speculated that at pH 12, the catalyst surface assumes very high negative potential, and a thin film of MB dye may form on the catalyst surface because of the strong electrostatic force between the high negatively charged surface and cationic dye MB. This thin film inhibits the light penetration to the catalyst surface and thus hinders the activation of the catalyst. In contrast, at lower pH, the adsorption of MB dye decreases due to the repulsion force between positively charged metal oxide NCs and the cationic dye MB and that results in a severe decrease in degradation efficiency. A similar trend is also reported in the literature [78,79].

The degradation efficiency also depends on the dose of the photocatalysts. The percentage degradation of MB after 20 min of UV light irradiation at different doses of 2 wt% CeO_2/TiO_2 NCs is presented in Fig. S2B. As shown in Fig. S2B, the percentage degradation of MB increases from 71% to 97% when the photocatalyst dose is increased from 0.5 to 1.5 g/L. Further increase in catalyst dose results in a decrease in the degradation percentage. As 96% degradation of dye is achieved at a dose of 1 g/L, it is considered as the optimum dose in this study. The improved degradation efficiency is attributed to the formation of more hydroxyl radicals resulting from the more active sites on the surface of NCs with increasing doses of catalysts. On the other hand, a high dose of photocatalyst beyond a certain limit increases the opacity of the solution and hinders the light penetration by scattering the light, and that leads to a decrease in degradation efficiency [85,86]. The loss in surface area by agglomeration (particle–particle interactions) at high solid concentration also decreased the degradation efficiency [86]. In addition, the photocatalyst is reused several times to confirm the stability in repeated uses. No significant loss in degradation efficiency is observed in three successive use of 2 wt% CeO_2/TiO_2 NCs, which evidences the stability and reusability of the prepared photocatalysts (Fig. 6B). The degradation efficiencies of 2 wt%

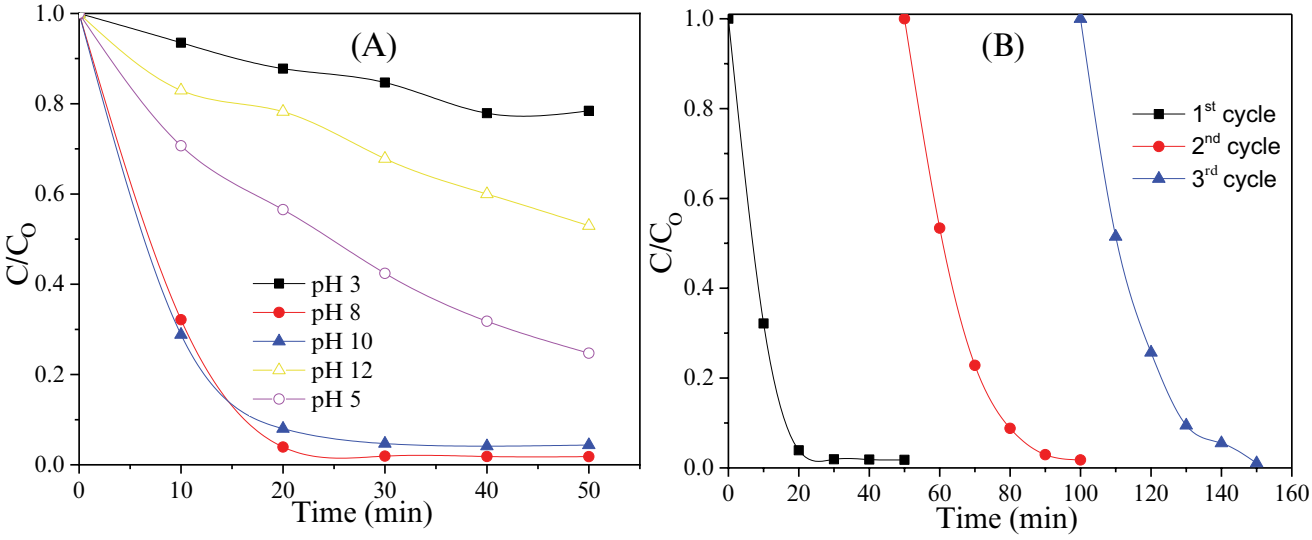

Fig. 6. (A) Effect of pH on the photodegradation efficiency of 2 wt% CeO_2/TiO_2 NCs (initial dye solution concentration = 10 mg /L; solution volume = 100 mL, catalyst dose = 1 g/L); (B) repeated runs in the photodegradation of MB using the 2 wt% CeO_2/TiO_2 photocatalyst under UV-light irradiation (initial dye solution concentration = 10 mg/L; volume = 100 mL; pH = 8; catalyst dose = 1 g/L; irradiation time = 50 min).

CeO_2/TiO_2 NCs after 40 min irradiation for three successive uses are found to be 98.15%, 97.06%, and 95%, respectively.

3.3.1. Photocatalytic degradation mechanism

The enhanced degradation efficiency of heterostructure CeO_2/TiO_2 NCs can be rationalized by band alignment at the interface between CeO_2 and TiO_2 nanoparticles. The conduction band (CB) and the valence band (VB) offsets existing at the interface spatially transfer photogenerated electron-holes in opposite direction, and thus reduce the charge recombination and consequently, increase the degradation efficiency. In this context, the positions of CB and VB edges of the constituent semiconductors determine the direction of the transfer of photogenerated electrons and holes. The position of CB and VB edges of CeO_2 and TiO_2 can be determined by the following Mulliken electronegativity equation [88]:

$$E_{CB} = \chi - E_e - 0.5E_g \quad (9)$$

$$E_{VB} = \chi - E_e + 0.5E_g \quad (10)$$

where χ, E_{VB}, E_{CB}, and E_g are the electronegativity, the valence band edge potential, conduction band edge potential, and the bandgap energy of the semiconductor, respectively. E_e denotes the free electron energy on the hydrogen scale (4.5 eV). The value of χ for a particular semiconductor can be obtained from the geometric means of the electronegativities of the constituent atoms in the semiconductor. The arithmetic mean of electron affinity and ionization potential of an element gives the electronegativity of the element. The electron affinity and ionization potential of oxygen, cerium, and titanium are reported as 1.46, 0.95, and 0.08 eV and 13.6, 5.47, and 6.8 eV, respectively [89,90]. Thus, the values of χ for CeO_2 and TiO_2 are estimated to be 5.56 and 5.79 eV, respectively. The calculated band gap energy of TiO_2 is 3.25 eV. The bandgap energy of CeO_2 is reported to be 3.00 eV [91,92]. The estimated values of E_{CB} and E_{VB} for TiO_2 were found to be 0.34 and 2.91 eV, respectively. On the other hand, E_{CB} and E_{VB} for CeO_2 are calculated to be –0.44 and 2.56 eV, respectively. Thus, both the conduction band edge and valence band edge of CeO_2 are more negative than those of TiO_2. Based on the calculated band edge position, the band alignment of the CeO_2/TiO_2 NCs was schematically represented in Fig. 7. It is obvious from Fig. 7 that there exist both valence band and conduction band offsets at the interface of CeO_2 and TiO_2 nanoparticles in CeO_2/TiO_2 NCs. When the CeO_2/TiO_2 NCs are illuminated with UV light, the electrons in valence bands of both the semiconductor oxides are excited to jump to the conduction bands with the concurrent generation of the equal number of holes in valence bands. As the CB edge and the VB edge of CeO_2 are more negative than the corresponding edges of TiO_2, the electrons in the CB of CeO_2 are injected into that of TiO_2 and at the same time holes in the VB of TiO_2 are inserted into the VB of CeO_2. This process of transferring photogenerated electrons and holes is illustrated in Fig. 7. Thus, photogenerated electrons and holes are transferred in opposite directions in the two semiconductors. Thus, photogenerated electrons and holes are efficiently separated due to their vector transfer to TiO_2 and CeO_2, respectively, providing a high propensity of charge carriers with suitably long lifetimes to participate in the redox reaction and hence reducing the recombination of photogenerated charge carriers. The enhanced photocatalytic degradation efficiency has attributed the reduction of charge carrier recombination of the CeO_2/TiO_2 NC system compared to their individual contribution.

The photocatalytic decomposition of MB can be explained by the following reactions:

$$CeO_2/TiO_2 + h\nu \rightarrow e^-(TiO_2) + h^+(CeO_2) \quad (11)$$

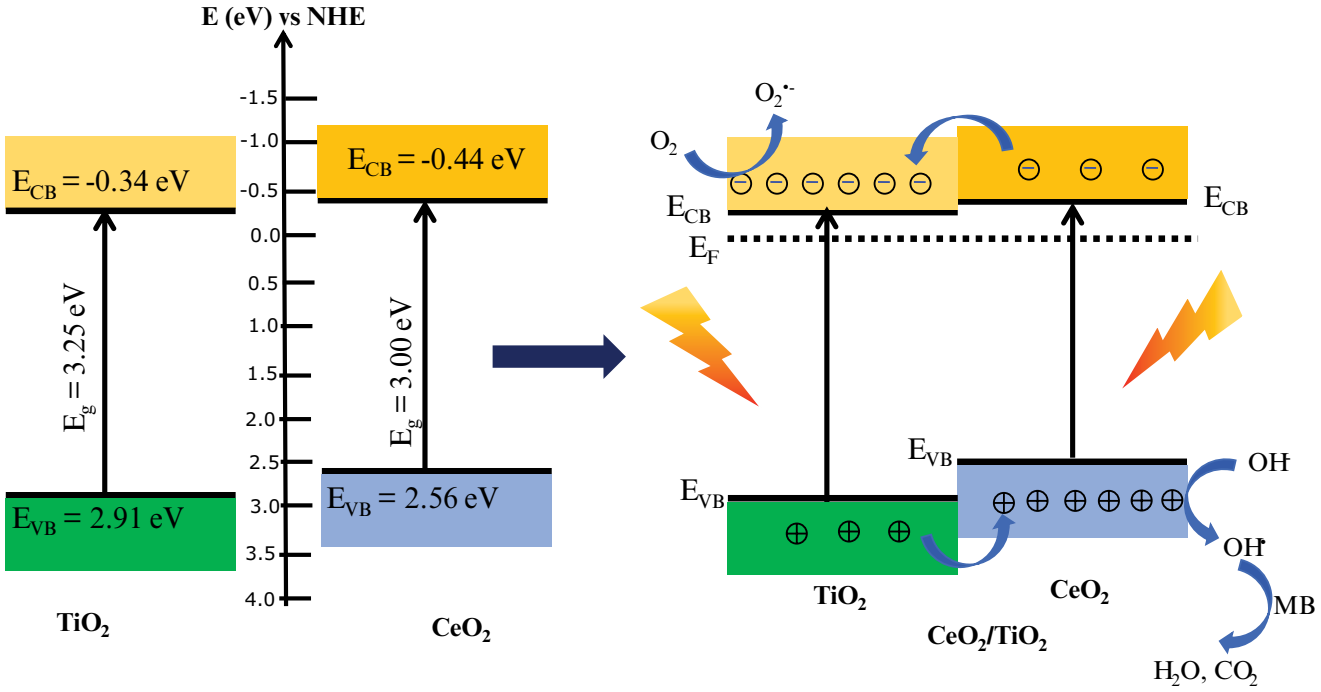

Fig. 7. Band alignment and the probable charge transfer mechanism of heterostructure CeO_2/TiO_2 NCs.

$$h^+(CeO_2) + OH^- \rightarrow OH^\circ(CeO_2) \quad (12)$$

$$e^-(TiO_2) + O_2 \rightarrow O_2^{\bullet-}(TiO_2) \quad (13)$$

$$O_2^{\bullet-}(TiO_2) + H_2O \rightarrow HO_2^\circ(TiO_2) + OH^- \quad (14)$$

$$HO_2^\circ(TiO_2) + H_2O \rightarrow H_2O_2(TiO_2) + OH^\circ(TiO_2) \quad (15)$$

$$H_2O_2 \rightarrow 2OH^\circ(TiO_2) \quad (16)$$

$$OH^\circ(TiO_2) + MB(TiO_2) \rightarrow \text{degradation products} \quad (17)$$

$$OH^\circ(CeO_2) + MB(CeO_2) \rightarrow \text{degradation products} \quad (18)$$

The holes in the VB of CeO_2 react with the hydroxyl groups (or H_2O) on the surface of CeO_2 to produce the hydroxyl radical species ($OH^\bullet$) [78]. In contrast, electrons in the CB of TiO_2 migrate to the active sites on the surface of TiO_2 and react with adsorbed O_2 to generate superoxide radials anion ($O_2^{\bullet-}$) which in turn react with water (H_2O) to produce hydroxyl radicals ($OH^\bullet$) [65]. The $OH^\bullet$ is a strong oxidizing agent which completely mineralizes organic compounds (herein MB dye) to the final degradation products CO_2 and H_2O [26,65].

The degradation products, CO_2 and H_2O, are confirmed by COD analysis. As a result of the photocatalytic degradation, the colored solution of the dye might turn into a colorless one. But the color change does not indicate the formation of CO_2 and H_2O. During photocatalytic degradation, the chromophore groups of organic compounds may break down producing low molecular weight colorless organic products. The low molecular weight colorless compounds are examined by COD analysis. If the degradation products are colorless organic compounds there would be no significant change in the COD value after photocatalytic degradation. The result of the COD analysis is presented in Fig. 8. As seen in Fig. 8, the COD value of the MB solution before degradation was about 33 mg/L. On the other hand, no measurable COD value of the

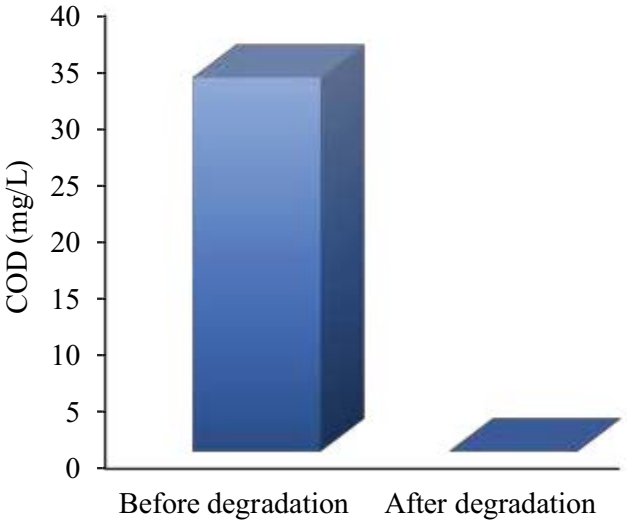

Fig. 8. COD values of MB before and after photocatalytic degradation with CeO_2/TiO_2 NCs.

sample is observed after photocatalytic degradation asserting that the MB is completely mineralized to CO_2 and H_2O.

4. Conclusion

Mesoporous heterostructure CeO_2/TiO_2 NCs are successfully synthesized via a simple solid-state reaction method at 500°C, and used as heterogeneous photocatalysts for the decomposition of methylene blue (MB) dye from aqueous solution under UV light irradiation. The CeO_2/TiO_2 NCs containing 2 wt% CeO_2 exhibit the highest MB degradation efficiency compared to pure TiO_2 and reference TiO_2 (P25). The band offsets at the interface of CeO_2 and TiO_2 NPs reduce the photogenerated charge recombination resulting in enhanced degradation efficiency of CeO_2/TiO_2 NCs. The basic media is favorable for the degradation of MB with CeO_2/TiO_2 NCs. In addition, repeated use of CeO_2/TiO_2 NCs does not show an appreciable reduction of the photocatalytic degradation efficiency certifying the stability and reusability of the photocatalysts. Therefore, the heterostructure CeO_2/TiO_2 NCs exhibit outstanding properties for the photocatalytic remediation of effluent-containing organic pollutants.

Compliance with ethical standards

Conflict of interest: The corresponding author declares on behalf of all authors that they have no known competing financial interests or personal relationships that could have appeared to influence the work reported in this paper.

Acknowledgments

This work was financially supported by the Ministry of Science and Technology, Government of the People's Republic of Bangladesh (Grant No. EAS435).

References

[1] F. Mashkoor, A. Nasar, Inamuddin, A.M. Asiri, Exploring the reusability of synthetically contaminated wastewater containing crystal violet dye using *Tectona grandis* sawdust as a very low-cost adsorbent, Sci. Rep., 8 (2018) 8314 (1–16), doi: 10.1038/s41598-018-26655-3.

[2] M.R. Islam, N.G. Das, P. Barua, M.B. Hossain, S. Venkatramanan, S.Y. Chung, Environmental assessment of water and soil contamination in Rajakhali Canal of Karnaphuli River (Bangladesh) impacted by anthropogenic influences: a preliminary case study, Appl. Water Sci., 7 (2017) 997–1010.

[3] M.J. Uddin, Y.K. Jeong, Urban river pollution in Bangladesh during last 40 years: potential public health and ecological risk, present policy, and future prospects toward smart water management, Heliyon, 7 (2021) e06107 (1–23), doi: 10.1016/j.heliyon.2021.e06107.

[4] M.Z. Bin Mukhlish, Y. Horie, T. Nomiyama, Flexible alumina-silica nanofibrous membrane and its high adaptability in reactive red-120 dye removal from water, Water Air Soil Pollut., 228 (2017) 371 (1–16), doi: 10.1007/s11270-017-3546-7.

[5] M. Imran, D.E. Crowley, A. Khalid, S. Hussain, M.W. Mumtaz, M. Arshad, Microbial biotechnology for decolorization of textile wastewaters, Rev. Environ. Sci. Biotechnol., 14 (2015) 73–92.

[6] M.S. Tsuboy, J.P.F. Angeli, M.S. Mantovani, S. Knasmüller, G.A. Umbuzeiro, L.R. Ribeiro, Genotoxic, mutagenic and cytotoxic effects of the commercial dye CI Disperse Blue 291 in the human hepatic cell line HepG2, Toxicol. In Vitro, 21 (2007) 1650–1655.

[7] M.R. Torres, C.G. Bouzán, M. Crespi, Combination of coagulation–flocculation and nanofiltration techniques for dye removal and water reuse in textile effluents, Desalination, 252 (2010) 53–59.

[8] M.Z.B. Mukhlish, M.R. Khan, M.S. Islam, M.I. Nazir, J.S. Snigdha, R. Akter, H. Ahmad, Decolorization of reactive dyes from aqueous solution using combined coagulation-flocculation and photochemical oxidation (UV/H_2O_2), Sustainable Chem. Eng., 1 (2020) 51–61.

[9] I. Friha, M. Bradai, D. Johnson, N. Hilal, S. Loukil, F.B. Amor, F. Feki, J. Han, H. Isoda, S. Sayadi, Treatment of textile wastewater by submerged membrane bioreactor: *in vitro* bioassays for the assessment of stress response elicited by raw and reclaimed wastewater, J. Environ. Manage., 160 (2015) 184–192.

[10] M.T. Uddin, M.A. Islam, S. Mahmud, M. Rukanuzzaman, Adsorptive removal of methylene blue by tea waste, J. Hazard. Mater., 164 (2009) 53–60.

[11] A. Rathi, S. Basu, S. Barman, Adsorptive removal of fipronil from its aqueous solution by modified zeolite HZSM-5: equilibrium, kinetic and thermodynamic study, J. Mol. Liq., 283 (2019) 867–878.

[12] A. Rathi, S. Basu, S. Barman, Structural framework effect of various CeO_2-loaded zeolites on the adsorptive removal of fipronil, J. Environ. Chem. Eng., 9 (2021) 105167, doi: 10.1016/j.jece.2021.105167.

[13] A. Riga, K. Soutsas, K. Ntampegliotis, V. Karayannis, G. Papapolymerou, Effect of system parameters and of inorganic salts on the decolorization and degradation of Procion H-exl dyes. Comparison of H_2O_2/UV, Fenton, UV/Fenton, TiO_2/UV and TiO_2/UV/H_2O_2 processes, Desalination, 211 (2007) 72–86.

[14] S.S. Kalra, S. Mohan, A. Sinha, G. Singh, Advanced oxidation processes for treatment of textile and dye wastewater: a review, IPCBEE, 4 (2011) 271–275.

[15] B.N. Kumar, Y. Anjaneyulu, V. Himabindu, Comparative studies of degradation of dye intermediate (H-acid) using TiO_2/UV/H_2O_2 and photo-Fenton process, J. Chem. Pharm. Res., 3 (2011) 718–731.

[16] A.O. Ibhadon, P. Fitzpatrick, Heterogeneous photocatalysis: recent advances and applications, Catalysts, 3 (2013) 189–218.

[17] S. Ahmed, M.G. Rasul, W.N. Martens, R. Brown, M.A. Hashib, Advances in heterogeneous photocatalytic degradation of phenols and dyes in wastewater: a review, Water Air Soil Pollut., 215 (2011) 3–29.

[18] S.N. Ahmed, W. Haider, Heterogeneous photocatalysis and its potential applications in water and wastewater treatment: a review, Nanotechnology, 29 (2018) 342001 (1–30), doi: 10.1088/1361-6528/aac6ea.

[19] A. Fujishima, K. Honda, Electrochemical photolysis of water at a semiconductor electrode, Nature, 238 (1972) 37–38.

[20] C.G. Lee, H. Javed, D. Zhang, J.H. Kim, P. Westerhoff, Q. Li, P.J.J. Alvarez, Porous electrospun fibers embedding TiO_2 for adsorption and photocatalytic degradation of water pollutants, Environ. Sci. Technol., 52 (2018) 4285–4293.

[21] D. Chen, Y. Cheng, N. Zhou, P. Chen, Y. Wang, K. Li, S. Huo, P. Cheng, P. Peng, R. Zhang, L. Wang, H. Liu, Y. Liu, R. Ruan, Photocatalytic degradation of organic pollutants using TiO_2-based photocatalysts: a review, J. Cleaner Prod., 268 (2020) 1–14, doi: 10.1016/j.jclepro.2020.121725.

[22] Q. Sun, K. Li, S. Wu, B. Han, L. Sui, L. Dong, Remarkable improvement of TiO_2 for dye photocatalytic degradation by a facile post-treatment, New J. Chem., 44 (2020) 1942–1952.

[23] M.Z.B. Mukhlish, F. Najnin, M.M. Rahman, M.J. Uddin, Photocatalytic degradation of different dyes using TiO_2 with high surface area: a kinetic study, J. Sci. Res., 5 (2013) 301–314.

[24] A.L. Linsebigler, G. Lu, J.T. Yates, Photocatalysis on TiO_2 surfaces: principles, mechanisms, and selected results, Chem. Rev., 95 (1995) 735–758.

[25] N. Laid, N. Bouanimba, R. Zouaghi, T. Sehili, Comparative study on photocatalytic decolorization of an anionic and a cationic dye using different TiO_2 photocatalysts, Desal. Water Treat., 57 (2016) 19357–19373.

[26] M.T. Uddin, Y. Nicolas, C. Olivier, T. Toupance, M.M. Müller, H.J. Kleebe, K. Rachut, J. Ziegler, A. Klein, W. Jaegermann, Preparation of RuO_2/TiO_2 mesoporous heterostructures and rationalization of their enhanced photocatalytic properties by band alignment investigations, J. Phys. Chem. C, 117 (2013) 22098–22110.
[27] B. Barrocas, O.C. Monteiro, M.R. Nunes, A.J. Silvestre, Influence of Re and Ru doping on the structural, optical and photocatalytic properties of nanocrystalline TiO_2, SN Appl. Sci., 1 (2019) 556, doi: 10.1007/s42452-019-0567-4.
[28] D. John, A.S. Rajalakshmi, R.M. Lopez, V.S. Achari, TiO_2-reduced graphene oxide nanocomposites for the trace removal of diclofenac, SN Appl. Sci., 2 (2020) 840, doi: 10.1007/s42452-020-2662-y.
[29] K. Musaev, D. Mirkhamitova, A. Yarbekov, S. Nurmanov, K. Akbarov, O. Ruzimuradov, Facile synthesis of SiO_2–TiO_2 photocatalyst nanoparticles for degradation of phenolic water pollutants, SN Appl. Sci., 1 (2019) 1164, doi: 10.1007/s42452-019-1192-y.
[30] N. Shafeei, G. Asadollahfardi, G. Moussavi, M.M.A. Boojar, Degradation of ibuprofen in the photocatalytic process with doped TiO_2 as catalyst and UVA-LED as existing source, Desal. Water Treat., 142 (2019) 341–352.
[31] S.B. Chergui, H. Zemmouri, M. Chabani, A. Bensmaili, TiO_2-photocatalyzed degradation of tetracycline: kinetic study, adsorption isotherms, mineralization and toxicity reduction, Desal. Water Treat., 57 (2016) 16670–16677.
[32] A. Wold, Photocatalytic properties of TiO_2, Chem. Mater., 5 (1993) 280–283.
[33] M.T. Uddin, Y. Nicolas, C. Olivier, W. Jaegermann, N. Rockstroh, H. Junge, T. Toupance, Band alignment investigations of heterostructure NiO/TiO_2 nanomaterials used as efficient heterojunction earth-abundant metal oxide photocatalysts for hydrogen production, Phys. Chem. Chem. Phys., 19 (2017) 19279–19288.
[34] J. Liu, Y. Li, J. Ke, S. Wang, L. Wang, H. Xiao, Black NiO-TiO_2 nanorods for solar photocatalysis: recognition of electronic structure and reaction mechanism, Appl. Catal., B, 224 (2018) 705–714.
[35] K. Salehi, B. Shahmoradi, A. Bahmani, M. Pirsaheb, H.P. Shivaraju, Optimization of reactive black 5 degradation using hydrothermally synthesized NiO/TiO_2 nanocomposite under natural sunlight irradiation, Desal. Water Treat., 57 (2016) 25256–25266.
[36] D. Toloman, O. Pana, M. Stefan, A. Popa, C. Leostean, S. Macavei, D. Silipas, I. Perhaita, M.D. Lazar, L.B. Tudoran, Photocatalytic activity of SnO_2–TiO_2 composite nanoparticles modified with PVP, J. Colloid Interface Sci., 542 (2019) 296–307.
[37] Talinungsang, N. Paul, D.D. Purkayastha, M.G. Krishna, TiO_2/SnO_2 and SnO_2/TiO_2 heterostructures as photocatalysts for degradation of stearic acid and methylene blue under UV irradiation, Superlattices Microstruct., 129 (2019) 105–114.
[38] M. Gholami, M.S. Siboni, M. Farzadkia, J.K. Yang, Synthesis, characterization, and application of ZnO/TiO_2 nanocomposite for photocatalysis of a herbicide (Bentazon), Desal. Water Treat., 57 (2016) 13632–13644.
[39] M.T. Uddin, O. Babot, L. Thomas, C. Olivier, M. Redaelli, M.D. Arienzo, F. Morazzoni, W. Jaegermann, N. Rockstroh, H. Junge, T. Toupance, New insights into the photocatalytic properties of RuO_2/TiO_2 mesoporous heterostructures for hydrogen production and organic pollutant photodecomposition, J. Phys. Chem. C, 119 (2015) 7006–7015.
[40] W. Subramonian, T.Y. Wu, S.P. Chai, Photocatalytic degradation of industrial pulp and paper mill effluent using synthesized magnetic Fe_2O_3-TiO_2: treatment efficiency and characterizations of reused photocatalyst, J. Environ. Manage., 187 (2017) 298–310.
[41] M. Nasirian, C.F.B. Lecompte, M. Mehrvar, Photocatalytic efficiency of Fe_2O_3/TiO_2 for the degradation of typical dyes in textile industries: effects of calcination temperature and UV-assisted thermal synthesis, J. Environ. Manage., 196 (2017) 487–498.
[42] F. Asgharzadeh, M. Gholami, A.J. Jafari, M. Kermani, H. Asgharnia, R.R. Kalantary, Heterogeneous photocatalytic degradation of metronidazole from aqueous solutions using Fe_3O_4/TiO_2 supported on biochar, Desal. Water Treat., 175 (2020) 304–315.
[43] N. Yaacob, A.F. Ismail, G.P. Sean, N.A.M. Nazri, Structural and photocatalytic properties of co-doped hybrid ZrO_2–TiO_2 photocatalysts, SN Appl. Sci., 1 (2019) 252, doi: 10.1007/s42452-019-0247-4.
[44] W. Li, H. Ding, H. Ji, W. Dai, J. Guo, G. Du, Photocatalytic degradation of tetracycline hydrochloride via a CdS-TiO_2 heterostructure composite under visible light irradiation, Nanomaterials, 8 (2018) 415 (1–12), doi: 10.3390/nano8060415.
[45] F.C. Chiu, C.M. Lai, Optical and electrical characterizations of cerium oxide thin films, J. Phys. D: Appl. Phys., 43 (2010) 075104 (1–5), doi: 10.1088/0022-3727/43/7/075104.
[46] M.F. Bekheet, M. Grünbacher, L. Schlicker, A. Gili, A. Doran, J.D. Epping, A. Gurlo, B. Klötzer, S. Penner, On the structural stability of crystalline ceria phases in undoped and acceptor-doped ceria materials under in situ reduction conditions, CrystEngComm, 21 (2019) 145–154.
[47] H. Gao, B. Qiao, T.J. Wang, D. Wang, Y. Jin, Cerium oxide coating of titanium dioxide pigment to decrease its photocatalytic activity, Ind. Eng. Chem. Res., 53 (2014) 189–197.
[48] T. Seadira, G. Sadanandam, T.A. Ntho, X. Lu, C.M. Masuku, M. Scurrell, Hydrogen production from glycerol reforming: conventional and green production, Rev. Chem. Eng., 34 (2018) 695–726.
[49] S.A.A.R. Sayyed, N.I. Beedri, V.S. Kadam, H.M. Pathan, Rose bengal-sensitized nanocrystalline ceria photoanode for dye-sensitized solar cell application, Bull. Mater. Sci., 39 (2016) 1381–1387.
[50] R. Saravanan, S. Joicy, V.K. Gupta, V. Narayanan, A. Stephen, Visible light induced degradation of methylene blue using CeO_2/V_2O_5 and CeO_2/CuO catalysts, Mater. Sci. Eng., C, 33 (2013) 4725–4731.
[51] M. Humayun, Z. Hu, A. Khan, W. Cheng, Y. Yuan, Z. Zheng, Q. Fu, W. Luo, Highly efficient degradation of 2,4-dichlorophenol over CeO_2/g-C_3N_4 composites under visible-light irradiation: detailed reaction pathway and mechanism, J. Hazard. Mater., 364 (2019) 635–644.
[52] O. Ola, M.M.M. Valer, Review of material design and reactor engineering on TiO_2 photocatalysis for CO_2 reduction, J. Photochem. Photobiol., C, 24 (2015) 16–42.
[53] S. Ghasemi, S.R. Setayesh, A.H. Yangjeh, M.R.H. Nezhad, M.R. Gholami, Assembly of CeO_2–TiO_2 nanoparticles prepared in room temperature ionic liquid on graphene nanosheets for photocatalytic degradation of pollutants, J. Hazard. Mater., 199–200 (2012) 170–178.
[54] F. Chen, P. Ho, R. Ran, W. Chen, Z. Si, X. Wu, D. Weng, Z. Huang, C. Lee, Synergistic effect of CeO_2 modified TiO_2 photocatalyst on the enhancement of visible light photocatalytic performance, J. Alloys Compd., 714 (2017) 560–566.
[55] Z. Fan, F. Meng, J. Gong, H. Li, Y. Hu, D. Liu, Enhanced photocatalytic activity of hierarchical flower-like CeO_2/TiO_2 heterostructures, Mater. Lett., 175 (2016) 36–39.
[56] T.M. Wandre, P.N. Gaikwad, A.S. Tapase, K.M. Garadkar, S.A. Vanalakar, P.D. Lokhande, R. Sasikala, P.P. Hankare, Sol–gel synthesized TiO_2–CeO_2 nanocomposite: an efficient photocatalyst for degradation of methyl orange under sunlight, J. Mater. Sci. Mater. Electron., 27 (2016) 825–833.
[57] H. Yang, K. Zhang, R. Shi, A. Tang, Sol–gel synthesis and photocatalytic activity of CeO_2/TiO_2 nanocomposites, J. Am. Ceram. Soc., 90 (2007) 1370–1374.
[58] L. Feng, H. Wang, X. Han, Preparation and catalytic performance of the CeO_2/TiO_2 composites, Mater. Res. Innovations, 19 (2015) 111–113.
[59] M. Nasr, W. Huang, C. Bittencourt, D. Cui, Y. Sun, L. Wang, N.G. Caperaa, Y. Ning, P. Song, P. Bonnet, C. Wang, Synthesis of BiOF/TiO_2 heterostructures and their enhanced visible-light photocatalytic activity, Eur. J. Inorg. Chem., 2020 (2020) 253–260.
[60] W. Zhang, X. Sun, B. Chen, Photocatalytic degradation of methyl orange on iron niobate prepared by solid-state reaction, Adv. Mater. Res., 113–116 (2010) 2021–2024.

[61] J. Xing, Z. Shan, K. Li, J. Bian, X. Lin, W. Wang, F. Huang, Photocatalytic activity of $Nb_2O_5/SrNb_2O_6$ heterojunction on the degradation of methyl orange, J. Phys. Chem. Solids, 69 (2008) 23–28.
[62] P. Ren, H. Fan, X. Wang, Solid-state synthesis of $Bi_2O_3/BaTiO_3$ heterostructure: preparation and photocatalytic degradation of methyl orange, Appl. Phys. A Mater. Sci. Process., 111 (2013) 1139–1145.
[63] A.A. Aziz, M.D.J. Ooi, M.J. Abdullah, The effects of oxygen-catalysed and heat treatment on the precipitation synthesised ZnO nanoparticles, J. Exp. Nanosci., 9 (2014) 27–40.
[64] B.M. Babić, S.K. Milonjić, M.J. Polovina, B.V. Kaludierović, Point of zero charge and intrinsic equilibrium constants of activated carbon cloth, Carbon, 37 (1999) 477–481.
[65] M.T. Uddin, M.E. Hoque, M.C. Bhoumick, Facile one-pot synthesis of heterostructure SnO_2/ZnO photocatalyst for enhanced photocatalytic degradation of organic dye, RSC Adv., 10 (2020) 23554–23565.
[66] T. Sreethawong, Y. Yamada, T. Kobayashi, S. Yoshikawa, Catalysis of nanocrystalline mesoporous TiO_2 on cyclohexene epoxidation with H_2O_2: effects of mesoporosity and metal oxide additives, J. Mol. Catal. A: Chem., 241 (2005) 23–32.
[67] B.M. Sollier, M. Bonne, N. Khenoussi, L. Michelin, E.E. Miró, L.E. Gómez, A. V. Boix, B. Lebeau, Synthesis and characterization of electrospun nanofibers of Sr–La–Ce oxides as catalysts for the oxidative coupling of methane, Ind. Eng. Chem. Res., 59 (2020) 11419–11430.
[68] H. Eskandarloo, A. Badiei, M.A. Behnajady, TiO_2/CeO_2 hybrid photocatalyst with enhanced photocatalytic activity: optimization of synthesis variables, Ind. Eng. Chem. Res., 53 (2014) 7847–7855.
[69] W. Promnopas, S. Promnopas, T. Phonkhokkong, T. Thongtem, D. Boonyawan, L. Yu, O. Wiranwetchayan, A. Phuruangrat, S. Thongtem, Crystalline phases and optical properties of titanium dioxide films deposited on glass substrates by microwave method, Surf. Coat. Technol., 306 (2016) 69–74.
[70] J.S. de Oliveira, M. Brondani, E.S. Mallmann, S.L. Jahn, E.L. Foletto, S. Silvestri, Preparation of highly efficient $CoFe_2O_4$/Zn_2SnO_4 composite photocatalyst for the degradation of rhodamine B dye from aqueous solution, Water Air Soil Pollut., 229 (2018) 386 (1–9), doi: 10.1007/s11270-018-4038-0.
[71] B.H. Chen, W. Liu, A. Li, Y.J. Liu, Z.S. Chao, A simple and convenient approach for preparing core-shell-like silica@ nickel species nanoparticles: highly efficient and stable catalyst for the dehydrogenation of 1,2-cyclohexanediol to catechol, Dalton Trans., 44 (2014) 1023–1038.
[72] C. Shifu, C. Lei, G. Shen, C. Gengyu, The preparation of coupled WO_3/TiO_2 photocatalyst by ball milling, Powder Technol., 160 (2005) 198–202.
[73] P. Kubelka, F. Munk, Ein Beitrag zur Optik der Farbanstriche, Z. Für Tech. Phys., 12 (1931) 593–601.
[74] R. López, R. Gómez, Band-gap energy estimation from diffuse reflectance measurements on sol-gel and commercial TiO_2: a comparative study, J. Sol-Gel Sci. Technol., 61 (2012) 1–7.
[75] G. Kortüm, J. Vogel, Die theorie der diffusen reflexion von Licht an pulverförmigen stoffen, Z. Fur Phys. Chem., 18 (1958) 110–122.
[76] D.Y. Lee, J.T. Kim, J.H. Park, Y.H. Kim, I.K. Lee, M.H. Lee, B.Y. Kim, Effect of Er doping on optical band gap energy of TiO_2 thin films prepared by spin coating, Curr. Appl. Phys., 13 (2013) 1301–1305.
[77] W. Zhang, N. Song, L.X. Guan, F. Li, M.M. Yao, Photocatalytic degradation of formaldehyde by nanostructured TiO_2 composite films, J. Exp. Nanosci., 11 (2016) 185–196.
[78] M.T. Uddin, Y. Nicolas, C. Olivier, T. Toupance, L. Servant, M.M. Müller, H.J. Kleebe, J. Ziegler, W. Jaegermann, Nanostructured SnO_2-ZnO heterojunction photocatalysts showing enhanced photocatalytic activity for the degradation of organic dyes, Inorg. Chem., 51 (2012) 7764–7773.
[79] M.T. Uddin, Y. Nicolas, C. Olivier, L. Servant, T. Toupance, S. Li, A. Klein, W. Jaegermann, Improved photocatalytic activity in RuO_2-ZnO nanoparticulate heterostructures due to inhomogeneous space charge effects, Phys. Chem. Chem. Phys., 17 (2015) 5090–5102.
[80] E.M. Mendoza, A.G. Nuñez-Briones, L.A.G. Cerda, R.D.P. Rodríguez, A.J.M. Luna, One-step synthesis of ZnO and Ag/ZnO heterostructures and their photocatalytic activity, Ceram. Int., 44 (2018) 6176–6180.
[81] M.A. Ahmed, E.E. El-Katori, Z.H. Gharni, Photocatalytic degradation of methylene blue dye using Fe_2O_3/TiO_2 nanoparticles prepared by sol-gel method, J. Alloys Compd., 553 (2013) 19–29.
[82] J.T. Adeleke, T. Theivasanthi, M. Thiruppathi, M. Swaminathan, T. Akomolafe, A.B. Alabi, Photocatalytic degradation of methylene blue by ZnO/$NiFe_2O_4$ nanoparticles, Appl. Surf. Sci., 455 (2018) 195–200.
[83] G.B. Vieira, H.J. José, M. Peterson, V.Z. Baldissarelli, P. Alvarez, R. de Fátima Peralta Muniz Moreira, CeO_2/TiO_2 nanostructures enhance adsorption and photocatalytic degradation of organic compounds in aqueous suspension, J. Photochem. Photobiol., A, 353 (2018) 325–336.
[84] J.P.S. Valente, P.M. Padilha, A.O. Florentino, Studies on the adsorption and kinetics of photodegradation of a model compound for heterogeneous photocatalysis onto TiO_2, Chemosphere, 64 (2006) 1128–1133.
[85] D. Monga, D. Ilager, N.P. Shetti, S. Basu, T.M. Aminabhavi, 2D/2d heterojunction of $MoS_2/g\text{-}C_3N_4$ nanoflowers for enhanced visible-light-driven photocatalytic and electrochemical degradation of organic pollutants, J. Environ. Manage., 274 (2020) 111208 (1–12), doi: 10.1016/j.jenvman.2020.111208.
[86] Aanchal, S. Barman, S. Basu, Complete removal of endocrine disrupting compound and toxic dye by visible light active porous $g\text{-}C_3N_4$/H-ZSM-$_5$ nanocomposite, Chemosphere, 241 (2020) 1–10, doi: 10.1016/j.chemosphere.2019.124981.
[87] S. Kaneco, M.A. Rahman, T. Suzuki, H. Katsumata, K. Ohta, Optimization of solar photocatalytic degradation conditions of bisphenol A in water using titanium dioxide, J. Photochem. Photobiol., A, 163 (2004) 419–424.
[88] X. Yong, M.A.A. Schoonen, The absolute energy positions of conduction and valence bands of selected semiconducting minerals, Am. Mineral., 85 (2000) 543–556.
[89] T. Andersen, H.K. Haugen, H. Hotop, Binding energies in atomic negative ions: III, J. Phys. Chem. Ref. Data, 28 (1999) 1511–1533.
[90] J.F. Liebman, Regularities and relations among ionization potentials of nontransition elements, J. Chem. Educ., 50 (1973) 831–834.
[91] M.G. Castaño, T.R. Reina, S. Ivanova, M.A. Centeno, J.A. Odriozola, Pt vs. Au in water-gas shift reaction, J. Catal., 314 (2014) 1–9.
[92] D. Channei, B. Inceesungvorn, N. Wetchakun, S. Ukritnukun, A. Nattestad, J. Chen, S. Phanichphant, Photocatalytic degradation of methyl orange by CeO_2 and Fe-doped CeO_2 films under visible light irradiation, Sci. Rep., 4 (2014) 5757 (1–7), doi: 10.1038/srep05757.

Supporting information

Fig. S2A depicted the results of the pH at the point of zero charge (pHpzc) estimation by the pH drift method. As shown in the Fig. S2, the ΔpH value was zero at the initial pH 7.60. Therefore, the pH at the point of zero charge (pHpzc) of 2 wt% CeO_2/TiO_2 nanocomposite was 7.60.

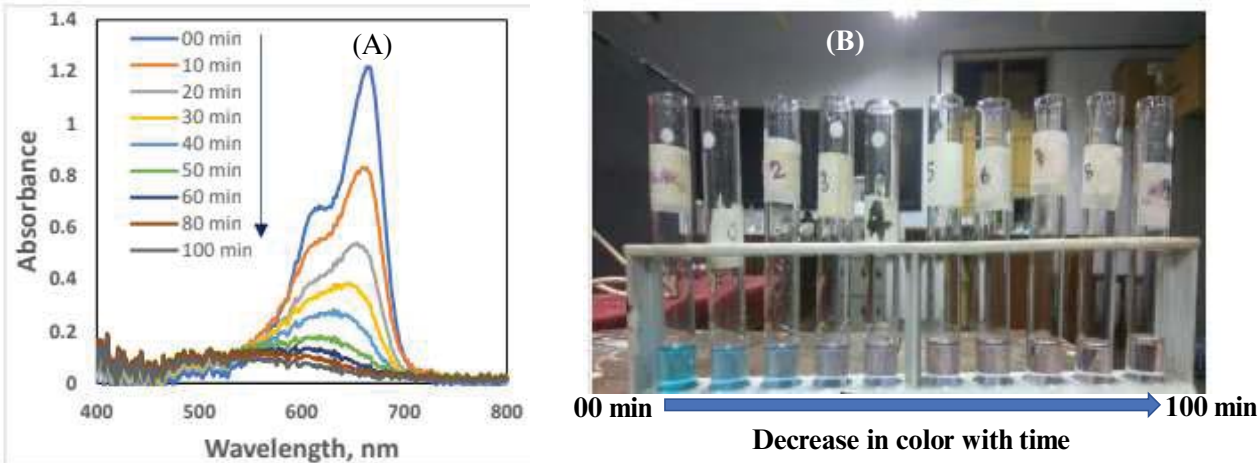

Fig. S1. Decrease in (A) absorbance and (B) color of MB solution with time under UV light irradiation.

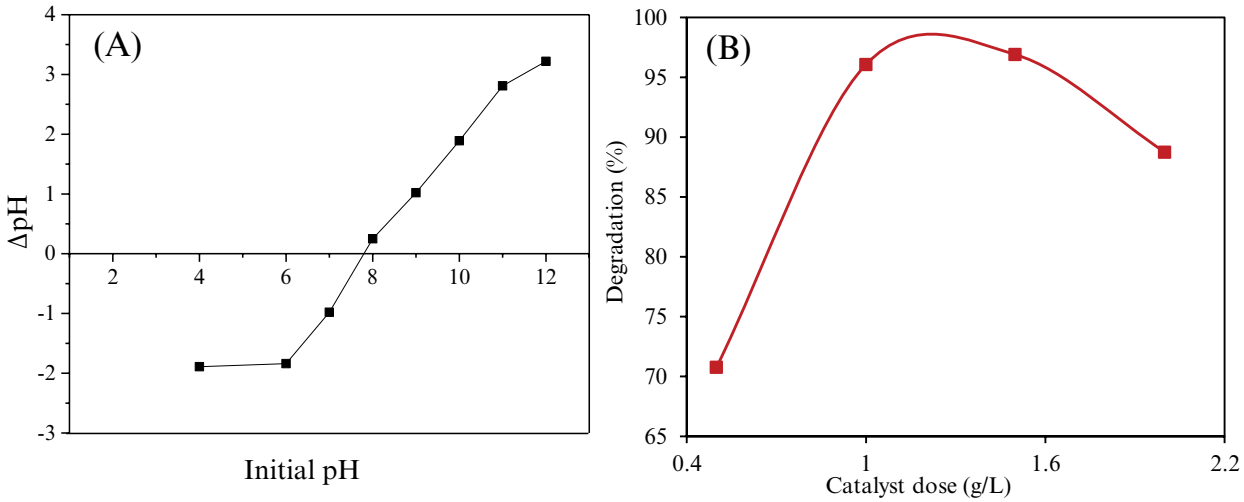

Fig. S2. (A) Determination of pHpzc of 2 wt% CeO_2/TiO_2 nanoparticles by the pH drift method and (B) effect of catalyst (2 wt% CeO_2/TiO_2 NCs) doses on the photodegradation of MB.

Table S1
Different methods for the synthesis CeO_2/TiO_2 NCs and their photocatalytic degradation efficiency for the degradation of different dyes

Synthetic method	Target dye	Catalyst loading	Time (min)	Light source	Degradation (%)	References
Hydrothermal	Rhodamine B	1 g/L	60	Vis	45	[1]
Hydrothermal	Rhodamine B	–	70	UV	90	[2]
Sol–gel	Reactive Red 195	0.08 g/L	120	UV	70	[3]
Sol–gel	Methyl orange	1 g/L	60	UV	98	[4]
Sol–gel	Methyl orange	1 g/L	90	UV	95	[5]
Impregnation	Methyl orange	0.1 g/L	105	UV	82	[6]
Hydrothermal	Methylene blue	0.5 g/L	160	UV	90	[7]
Precipitation	Methyl orange	0.1 g/L	25	UV	95	[8]

References

[1] F. Chen, P. Ho, R. Ran, W. Chen, Z. Si, X. Wu, D. Weng, Z. Huang, C. Lee, Synergistic effect of CeO_2 modified TiO_2 photocatalyst on the enhancement of visible light photocatalytic performance, J. Alloys Compd., 714 (2017) 560–566.

[2] Z. Fan, F. Meng, J. Gong, H. Li, Y. Hu, D. Liu, Enhanced photocatalytic activity of hierarchical flower-like CeO_2/TiO_2 heterostructures, Mater. Lett., 175 (2016) 36–39.

[3] S. Ghasemi, S.R. Setayesh, A.H. Yangjeh, M.R.H. Nezhad, M.R. Gholami, Assembly of CeO_2-TiO_2 nanoparticles prepared in room temperature ionic liquid on graphene nanosheets for photocatalytic degradation of pollutants, J. Hazard. Mater., 199–200 (2012) 170–178.

[4] T.M. Wandre, P.N. Gaikwad, A.S. Tapase, K.M. Garadkar, S.A. Vanalakar, P.D. Lokhande, R. Sasikala, P.P. Hankare, Sol–gel synthesized TiO_2–CeO_2 nanocomposite: an efficient photocatalyst for degradation of methyl orange under sunlight, J. Mater. Sci. Mater. Electron., 27 (2016) 825–833.

[5] H. Yang, K. Zhang, R. Shi, A. Tang, Sol-gel synthesis and photocatalytic activity of CeO_2/TiO_2 nanocomposites, J. Am. Ceram. Soc., 90 (2007) 1370–1374.

[6] L. Feng, H. Wang, X. Han, Preparation and catalytic performance of the CeO_2/TiO_2 composites, Mater. Res. Innov., 19 (2015) 111–113.

[7] G.B. Vieira, H.J. José, M. Peterson, V.Z. Baldissarelli, P. Alvarez, R. de Fátima Peralta Muniz Moreira, CeO_2/TiO_2 nanostructures enhance adsorption and photocatalytic degradation of organic compounds in aqueous suspension, J. Photochem. Photobiol., A, 353 (2018) 325–336.

[8] J. Tian, Y. Sang, Z. Zhao, W. Zhou, D. Wang, X. Kang, H. Liu, J. Wang, S. Chen, H. Cai, H. Huang, Enhanced photocatalytic performances of CeO_2/TiO_2 nanobelt heterostructures, Small, 9 (2013) 3864–3872.